nature communications

Article

https://doi.org/10.1038/s41467-024-52347-w

Multifunctional Magnetic Muscles for Soft Robotics

Received: 15 February 2024

Accepted: 2 September 2024

Published online: 10 September 2024

Check for updates

Minho Seong[1,4], Kahyun Sun[1,4], Somi Kim[1,4], Hyukjoo Kwon[1], Sang-Woo Lee[1], Sarath Chandra Veerla[1], Dong Kwan Kang[1], Jaeil Kim[1], Stalin Kondaveeti[1,2], Salah M. Tawfik[1,3], Hyung Wook Park[1] & Hoon Eui Jeong[1]

Despite recent advancements, artificial muscles have not yet been able to strike the right balance between exceptional mechanical properties and dexterous actuation abilities that are found in biological systems. Here, we present an artificial magnetic muscle that exhibits multiple remarkable mechanical properties and demonstrates comprehensive actuating performance, surpassing those of biological muscles. This artificial muscle utilizes a composite configuration, integrating a phase-change polymer and ferromagnetic particles, enabling active control over mechanical properties and complex actuating motions through remote laser heating and magnetic field manipulation. Consequently, the magnetic composite muscle can dynamically adjust its stiffness as needed, achieving a switching ratio exceeding 2.7×10^3. This remarkable adaptability facilitates substantial load-bearing capacity, with specific load capacities of up to 1000 and 3690 for tensile and compressive stresses, respectively. Moreover, it demonstrates reversible extension, contraction, bending, and twisting, with stretchability exceeding 800%. We leverage these distinctive attributes to showcase the versatility of this composite muscle as a soft continuum robotic manipulator. It adeptly executes various programmable responses and performs complex tasks while minimizing mechanical vibrations. Furthermore, we demonstrate that this composite muscle excels across multiple mechanical and actuation aspects compared to existing actuators.

Soft actuators and artificial muscles are gaining prominence as indispensable components for a wide range of applications, including soft robotics[1,2], exoskeletons[3], wearables[4,5], and biomedical devices[6]. Constructed from soft materials, these actuators provide inherent compliance, enabling their usage in uncontrolled and complex environments without requiring complex control algorithms[1,6]. However, soft materials commonly used in soft-bodied devices, such as silicones[7,8] (e.g., polydimethylsiloxane, Ecoflex, or Dragon Skin) and hydrogels[9], have limited mechanical properties. Their inherent softness restricts load-bearing capacity, force output, and resistance to fatigue or damage[10]. Additionally, the elastic nature of these materials results in undesired vibrations, posing challenges for the accurate control of specific operations[11].

To address these limitations, stiffness-tunable materials have been developed to achieve high deformability, force output, and load-bearing capacity. Examples include jamming materials[7,12], pneumatic

[1]Department of Mechanical Engineering, Ulsan National Institute of Science and Technology (UNIST), Ulsan, Republic of Korea. [2]Climate Change Cluster, University of Technology Sydney, Ultimo, Australia. [3]Egyptian Petroleum Research Institute (EPRI), Nasr City, Egypt. [4]These authors contributed equally: Minho Seong, Kahyun Sun, Somi Kim. e-mail: hoonejeong@unist.ac.kr

systems[13], low-melting-point alloys[14], and shape memory alloys[15]. However, these materials typically exhibit a narrow stiffness range and low specific load capacity. Additionally, many of these materials have limited intrinsic mechanical properties in terms of stretchability, toughness, and dynamic damping capacity. Moreover, they require complex wired connections for vacuum suction[16], pneumatic control[13], or Joule heating[15]. As such, magnetic soft materials are a promising candidate for soft robotics because of their simple, wireless controllability, rapid field responsiveness, and facile tunability of field direction and strength[17–21]. Furthermore, magnetic control can be decoupled from other stimuli, enabling multi-stimuli responsive actuators[22,23]. These actuators based on magnetic soft materials demonstrate programmable and versatile shape morphing. However, as with the aforementioned existing soft actuators, they also have limitations in terms of comprehensive mechanical and actuation performance.

Herein, we present a reconfigurable and adaptable soft magnetic muscle that outperforms the mechanical and actuating performance of biological muscles. These remarkable attributes are achieved by integrating a shape memory polymer and magnetic particles in a composite configuration. We demonstrate that the magnetic composite muscle can transition from a highly soft state (Young's modulus, E, of 110 kPa) to a rigid state (E of 296.9 MPa) by modulating photothermal stimuli, resulting in a stiffness switching ratio (SSR) exceeding 2.7×10^3. Consequently, the composite muscle can manipulate heavy objects with a maximum payload-to-weight ratio of up to 1000 and 3690 for tensile and compressive stresses, respectively. Moreover, it exhibits on-demand extension, contraction, bending, and twisting, with high stretchability exceeding 800% in its deformable state. These distinctive attributes enable the use of the magnetic composite muscle as a soft continuum robotic manipulator. It adeptly executes intricate and dexterous programmable responses while minimizing mechanical vibrations through remote laser heating and magnetic field control. We further demonstrate that the composite muscle displays a high maximum modulus (2.4 GPa), significant elongation at break (815%), appropriate damping ratio (1.348), high actuation strain rate (63.8% s^{-1}), impressive work density (129.5 kJ m^{-3}), and exceptional energy efficiency (90.9%).

Results

Monophasic magnetic composite muscle

An artificial magnetic muscle comprising a monophasic magnetic composite was designed to exhibit essential properties for soft robotics, e.g., wide-ranging variable stiffness, high load-bearing capacity, resilience, shape memory, remote actuation, and substantial actuation strain (Fig. 1a). Additionally, it was engineered to perform diverse motions, such as reversible extension, bending, and twisting (Fig. 1a).

The composite primarily consists of a polymer matrix and NdFeB microparticles (Fig. 1b). A copolymer of stearyl methacrylate and ethylene glycol dimethacrylate (poly(SMA-*co*-EGDMA)) serves as the hydrophobic, stimuli-responsive phase-changing component. The copolymer's long alkyl side chains form well-organized stacked crystals at room temperature, providing high mechanical strength and load-bearing capacity[24]. Furthermore, the combination of bottlebrushed architectures with numerous hydrophobic associations enables excellent shape memory behavior, allowing rapid transitions between rigid and soft states at elevated temperatures (Fig. 1bi)[25]. The NdFeB microparticles, grafted with octadecyltrichlorosilane (ODTS), form physical entanglements with the alkyl side chains of poly(SMA), creating hydrophobic interactions and a dual network in the composite (Fig. 1bii–iv, Supplementary Fig. 1, and Supplementary Note 1)[26]. Additionally, these microparticles serve as photothermal agents, enhancing phase transition behavior under heat and providing a rapid magnetic response to external magnetic fields[27–29].

Figure 1c illustrates the working mechanism of the monophasic composite muscle. Initially, the composites are in a rigid state at ambient temperature (Fig. 1ci). In this state, the crystallized alkyl side chains exhibit limited mobility, allowing them to withstand high external loads[30]. The crystalline structure is confirmed by the distinct isotropic scattering patterns observed through wide-angle X-ray scattering analysis (WAXS) (Fig. 1cii). When heated, the hydrophobic bonds between the alkyl chains relax thermally, and the composite transition to a deformable state with randomly arranged amorphous side chains (Fig. 1ci and Supplementary Fig. 2), as indicated by the blurred isotropic scattering pattern in the 2D WAXS (Fig. 1ciii). When actuated or stretched in the deformable state, the side chains align tightly, reducing the distance between each chain (Fig. 1civ). Upon removing the heat while maintaining tensile stress, the deformed shape is locked as the side chains recrystallize (Fig. 1cv).

We conducted dynamic mechanical analysis (DMA) on the composite while varying the loading concentrations of the magnetic particles (Supplementary Fig. 3). The storage modulus (G') exhibited a positive correlation with increasing particle content, indicating that the particles reinforced the polymer network[31]. However, the G' dropped significantly by approximately 2–3 orders of magnitude around the melting temperature (T_m) of 37.5 °C. This abrupt change could be attributed to the reversible phase change of the uniform side chains in the composite between the rigid and soft states[24]. The stiffness-changing ability of the composite was further evaluated by measuring the elastic modulus at both room temperature (25 °C, E_{rigid}) and elevated temperature (70 °C, E_{soft}) for varying magnetic particle contents (Fig. 1d). We defined the ratio of the elastic modulus in the rigid state (E_{rigid}, 25 °C) to that in the deformable state (E_{soft}, 70 °C) as the stiffness switching ratio (SSR = E_{rigid} / E_{soft}). The pristine copolymer without magnetic particles exhibited E_{rigid} and E_{soft} values of 75.8 MPa and 0.04 MPa, respectively, resulting in an SSR of 1.9×10^3. As the magnetic particle content increased, E_{rigid} also increased, reaching a maximum value of 296.9 MPa at 13 g of NdFeB. E_{soft} showed a similar trend, increasing with the particle content, but it reached its peak at 0.145 MPa for 11 g of NdFeB. Notably, the SSR reached a maximum of 2.7×10^3 with a NdFeB content of 13 g, spanning from a highly soft material state (110 kPa) to a rigid state (296.9 MPa).

We also evaluated the maximum strength, elongation at break, and toughness of the composite at both room and elevated temperatures for varying quantities of the magnetic particles (Supplementary Fig. 4). Considering the balanced performance in terms of elastic modulus, SSR, maximum strength, elongation at break, and toughness at two different temperature phases, we selected a composite with 11 g of NdFeB particles for the subsequent experiments (Supplementary Note 2). Figure 1e presents the energy density (u) and energy efficiency (η) of the composite during the loading and unloading cycles at various strains (100–500%) (Supplementary Fig. 5). The energy density increased with the applied strain, ultimately reaching an energy density of 0.852 MJ m^{-3} at 500% strain. The composite also demonstrated notable energy efficiency η, ranging from 85.2% to 90.9% for strains between 100% and 500%. Moreover, the composite subjected to strains exhibited rapid and full recovery to its original state in 1–1.7 s, ensuring a high actuation speed (maximum value of 63.8% s^{-1}) (Supplementary Fig. 6).

The monophasic magnetic composite also showed remarkable work and power density, achieving a work density of 129.5 kJ m^{-3} for 500% strain (Supplementary Fig. 7). Additionally, the composite exhibited ferromagnetic behavior with a saturation magnetization value of 358.4 kA m^{-1} at 11 g of NdFeB, enabling the remote control of the composite muscle (Supplementary Fig. 8a and Supplementary Note 3). Accordingly, our magnetic composite muscle demonstrated a balanced combination of various exceptional mechanical and actuating performances, surpassing not only the capabilities of biological systems but also outperforming several existing artificial muscles

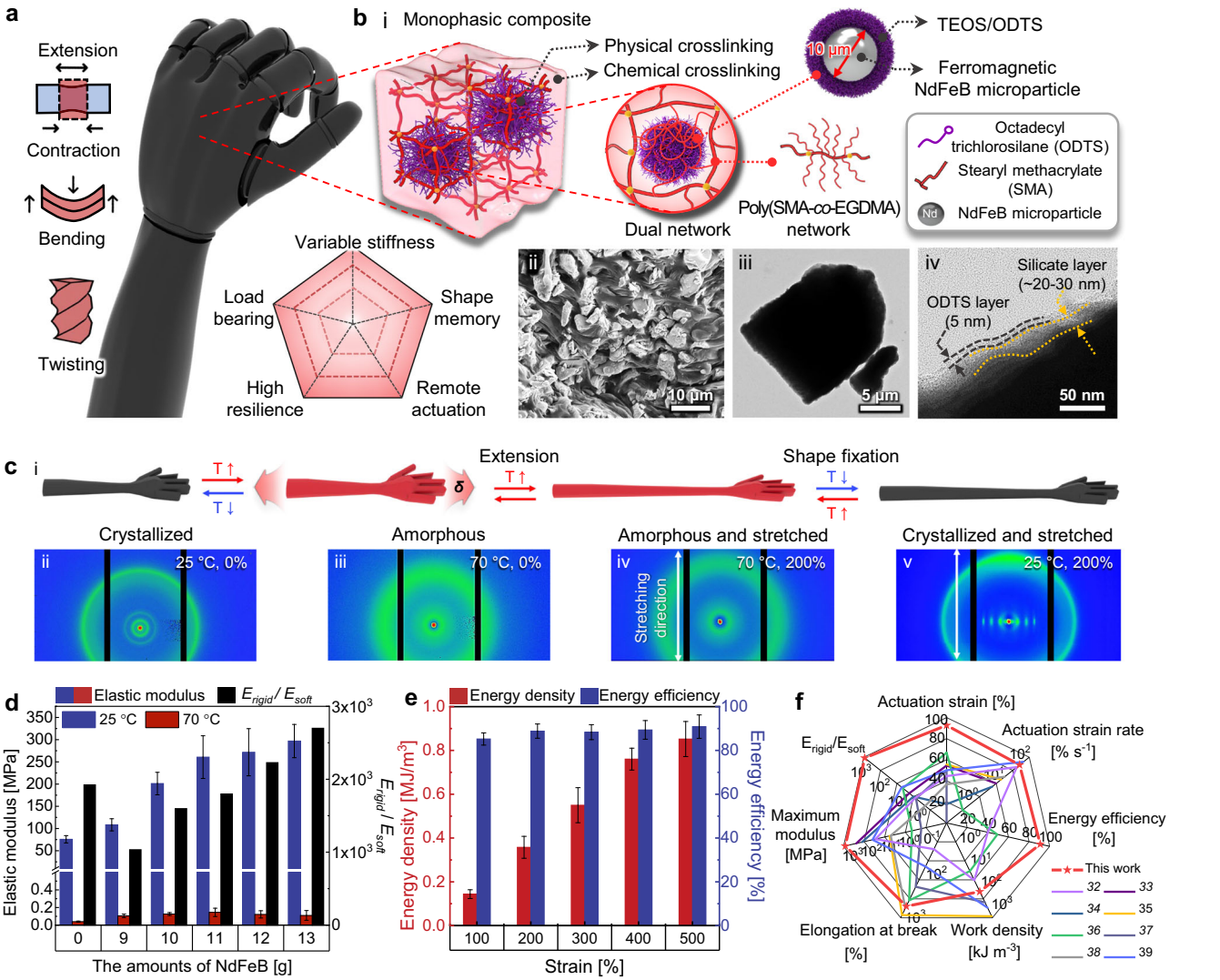

Fig. 1 | Design and properties of the monophasic composite muscle. a A schematic illustration depicting the concept of the monophasic composite muscle and its multifunctionalities. **b** (i) Chemical composition of the composite; (ii) SEM image showing the microstructures of the composite; (iii) low- and (iv) high-resolution TEM images of the NdFeB microparticles. **c** (i) Working mechanism of the poly(SMA-*co*-EGDMA) and (ii-v) WAXS analysis images of the composites under different conditions (crystallized, amorphous, amorphous and stretched, and crystallized and stretched). **d** Elastic moduli and stiffness switching ratio of the composites at 25 °C and 70 °C as a function of the amount of magnetic particles. **e** Energy density (u) and energy efficiency (η) of the composite during the loading and unloading cycles at various strains (100–500%). **f** Performance benchmark between the proposed magnetic composite muscle and previous artificial muscles. Error bars in each graph represent standard deviation, $n = 5$ independent samples.

(Fig. 1f, Supplementary Table 1, and Supplementary Notes 4, 5)[32–40]. Remarkably, after 100 cycles, all properties maintained at least 85.6% of their initial performance (Supplementary Fig. 9).

Reconfigurable and dual-responsive robotic hand

To demonstrate the versatility of the multifunctional monophasic composite muscle in soft robotics, we fabricated a field-responsive adaptable robotic hand (Fig. 2) using a molding process (Supplementary Fig. 10). Subsequently, the replicated robotic hand was magnetized while maintaining a curled shape (Fig. 2ai). Upon thermal heating, the magnetized robotic hand softened and reverted to a flat state due to the shape memory feature of the composite. In this deformable state, the robotic hand could undergo extensive stretching or generate dynamic actuating motion through magnetic torque ($\vec{\tau} = \vec{\mathbf{M}} \times \vec{\mathbf{B}}$, where $\mathbf{M}$ is the magnetization per volume, and $\mathbf{B}$ is the magnetic flux density) or magnetic force ($\vec{\mathbf{F}} = \nabla(\mathbf{M} \cdot \mathbf{B})$), induced by manipulating an external magnetic field (Fig. 2aii)[27]. Additionally, the robotic hand could lock into its deformed or actuated state by cooling to room temperature, demonstrating substantial mechanical strength and load-bearing capacity (Fig. 2aiii). The locked hand could revert to its initial unstretched state reversibly by heating owing to its resilience and shape memory property.

Figure 2b depicts a series of time-lapse images illustrating various operational motions of the robotic hand. Initially, the hand was in a locked state (Fig. 2bi and Supplementary Movie 1). Upon applying heat, the hand transitioned into a deformable state. Subsequently, when an external field was applied, the robotic fingers performed grasping motions. After removing this external field, the fingers returned to their original flat state. Leveraging this dynamic finger motion, the robotic hand could grasp and release a spherical object (Fig. 2bii and Supplementary Movie 2) or lift a heavy weight of 50–100 g (Fig. 2biii, Supplementary Fig. 11a and Supplementary Movie 3) using remote control by combining thermal stimuli from a laser (808 nm, power density: 2 W cm^{-2}) and magnetic stimuli.

Further examination revealed the remarkable load-bearing and resilient properties of the monophasic composite. The composite

https://doi.org/10.1038/s41467-024-52347-w

Fig. 2 | Reconfigurable and dual-responsive robotic hand made of the monophasic composite muscle. a A schematic illustration depicting the working mechanism of the robotic hand made of the monophasic composite. **b** (i) Time-lapse photographs demonstrating the grasping actuation capability of the robotic hand via photothermal and magnetic field control; (ii) time-lapse photographs showing the grasping and release of objects using the robotic hand; and (iii) time-lapse photographs showing the load-bearing capacity and shape-locking capability of the robotic hand. **c** Photographs showing the (i) robotic hand in the rigid state supporting a significant weight of 1 kg while maintaining a horizontal locked position without energy input, corresponding to a specific load capacity exceeding 100 and (ii) robotic hand in the deformable state sustaining a weight of 1 kg while being stretched downward by approximately 350% without any fracture. **d** Photographs showing the robotic hand supporting a weight of 200 g in an upper vertical posture and rigid state (i) without elongation and (ii) with 135% elongation.

robotic hand supported an impressive weight of 1 kg while maintaining a horizontal locked position without continuous energy input (Fig. 2ci), with a specific load capacity exceeding 100. In contrast, in the deformable state, the hand could sustain a weight of 1 kg while being stretched downward by approximately 350% without any fracture, demonstrating its mechanical robustness (Fig. 2cii). Notably, the robotic hand endured forces of up to 5 kg, which was 1000 times greater than its own weight (Supplementary Fig. 11b). This load-bearing capacity distinguishes it from many existing soft robotic systems with limited loading capacities. Furthermore, the composite displayed exceptional durability by withstanding the weight of a car (specific load capacity of 3690) or crushing hard objects without fracture, showing its remarkable yet adaptable mechanical properties (Supplementary Fig. 12, and Supplementary Movies 4 and 5). Additionally, the hand supported a weight of 200 g even while it was extended (~135%) in an upper vertical posture (Fig. 2d). These results demonstrate the multifaceted capabilities of the monophasic composite, encompassing remote actuation, shape memory, high resilience, variable stiffness, and exceptional load-bearing and shape-locking capacities within soft robotic systems.

Biphasic magnetic composite muscle

The magnetic composite muscle can be tailored to enhance its stretchability and damping capacity, expanding its range of applications. For example, soft robots with higher damping capacities can effectively dissipate accumulated energy and mitigate undesirable vibrations[11]. This improved damping capability allows for more precise control of soft robots during rapid actuation and offers protection against external shocks[41]. To achieve increased damping capacity and stretchability while maintaining exceptional material properties, we emulsified the monophasic magnetic composite into a hydrophilic phase polymer. This process, followed by in-situ polymerization, resulted in the formation of a biphasic composite (Fig. 3ai,ii, Supplementary Fig. 13, and Supplementary Note 6)[42]. The hydrophilic phase consisted of poly(*N*,*N*-dimethylacrylamide) (poly(DMAA)), alginate, and trivalent Al^{3+} ions, forming interpenetrated double network structures of poly(DMAA)-alginate/Al^{3+} (Fig. 3a). The dynamic reversible bonds, including hydrogen bonds within the double network and ionic bonds between the alginate and the Al^{3+} ions, facilitated the effective stress dissipation in the biphasic composite[43,44]. Consequently, the biphasic composite exhibited enhanced stretchability, deformability, and damping capacity[45,46]. Specifically, it could stretch over 800% strain, twist up to 360 degrees, and fold with a curvature of 5 mm (Fig. 3aii). While previous studies have demonstrated hydrogels or elastomers with ultra-high stretchability (ranging from 1000% to 30,000%)[44,47,48], the biphasic composite still surpasses the stretchability of many existing soft magnetic composites (300–460%)[23,49] and stiffness-variable polymers (290–740%)[50,51].

The microstructures of the biphasic composite were examined using three-dimensional nano-computed tomography (3D Nano-CT) and scanning electron microscopy (SEM) (Fig. 3b). As depicted, the hydrophobic phase (yellow color) and the hydrophilic phase (green color) were uniformly blended in the biphasic composite (Fig. 3bi, iii, v, and vi). Additionally, the NdFeB microparticles (purple color in Fig. 3bi,ii) were well dispersed within the hydrophobic phase. When subjected to stretching, the microstructures of the biphasic composites exhibited significant elongation along the direction of applied tension (Fig. 3bii, iv).

Next, we assessed the elongation at break and elastic moduli of the biphasic composite (Fig. 3c, d). We compared three different variations: the biphasic composite without alginate (DMAA), the biphasic composite with sodium alginate (SA) (DMAA-Alg), and the biphasic composite with Al^{3+} ions-coordinated alginate (DMAA-Alg/Al^{3+}) (see Supplementary Fig. 14 and Supplementary Note 7 for their chemical analyzes). The DMAA-Alg/Al^{3+} composite showed a higher elongation at break of 815% in the deformable state at 70 °C compared to the DMAA (483%) and DMAA-Alg (643%) composites (Fig. 3c and Supplementary Fig. 15). The DMAA-Alg/Al^{3+} also demonstrated a substantially enhanced elastic modulus compared to DMAA or DMAA-Alg (Fig. 3d). This enhancement can be attributed to the replacement of Na^{+} ions with Al^{3+} ions, which formed ionic bonds in alginates and increased the number of hydrogen bonds between alginate and Al^{3+}. The weak dynamic hydrogen bonds facilitated the dissipation of large strain energy, enhancing stretchability through rapid bond breakage and reformation. Meanwhile, the strong ionic bonds elevated the elastic modulus of the composite[52,53]. The DMAA-Alg/Al^{3+} also displayed the capacity to adjust stiffness, offering control over the mechanical modulus from soft (63 kPa) to stiff (38.5 MPa).

We then investigated the energy dissipation and strain recovery properties of the three different biphasic composites during deformations by conducting loading–unloading tests at various strain levels. The DMAA-Alg/Al^{3+} composite showed significantly enhanced energy dissipation capability at both 25 °C and 70 °C compared to both the DMAA and DMAA-Alg composites (Fig. 3e and Supplementary Fig. 16a). For instance, when subjected to a strain rate of 0.017 s^{-1} at 70 °C, the energy dissipation capacity of the DMAA-Alg/Al^{3+} composite reached to 300.5 kJ m^{-3} at 700% strain. Additionally, the DMAA-Alg/Al^{3+} composite displayed exceptional strain recovery capability of over 99% (Fig. 3f and Supplementary Fig. 16b). In contrast, the DMAA and DMAA-Alg samples exhibited permanent deformation during high stretching, with considerably lower strain recovery (Supplementary Fig. 17). Furthermore, the DMAA-Alg/Al^{3+} composite displayed excellent anti-fatigue behavior during the 1000th cyclic loading-unloading fatigue test after the 10 initial stabilization cycles (Fig. 3g and Supplementary Note 8).

Damping capacity

We assessed the damping capacity of three magnetic composite models—the monophasic, biphasic, and bilayer composites (Supplementary Fig. 18)—by observing their oscillation behavior during actuation (Fig. 4a). Each composite actuator, shaped like a square rod (500 mm in length, 3.2 mm in thickness, and 12 mm in width), was initially positioned vertically on the XZ plane with one end fixed. The midpoint of the actuators was locally heated using laser irradiation (808 nm, irradiance: 2 W cm^{-2}) to create a temporary deformable hinge. Upon applying an external magnetic field along the x-axis, all the composite actuators exhibited immediate folding motion at the hinge point.

Among the three actuator samples, the monophasic composite actuator demonstrated the fastest actuation (Fig. 4ai, b and Supplementary Movie 6). Upon application of a magnetic field, it initially reached the maximum bending angle within only 0.06 s. However, after the initial bending actuation, it displayed noticeable vibrations with a maximum peak-to-peak change in bending angle (θ) of 25.7°. The monophasic actuator took 0.29 s of settling time to stabilize within the error range of ±5% of its final steady-state θ value (88.4° for the monophasic actuator) (Fig. 4bi). The 5% error band is typically used to evaluate the damping property of systems[54]. In addition to the bending angle, the monophasic composite displayed noticeable oscillation in angular velocity (w), angular acceleration ($\boldsymbol{\alpha}$), and torque ($\mathbf{T_R}$) during the actuation (Supplementary Fig. 19). In contrast, the biphasic composite actuator achieved precise and gentle bending motion without significant vibrations, allowing the actuator to stabilize quickly during the bending motion, with a settling time of 0.25 s (Fig. 4aii, b, and Supplementary Movie 7). However, the biphasic composite actuator exhibited a lower bending capacity with a higher settling angle of 93.1°, displaying inferior bending motion compared to the monophasic composite actuator, because of the lower magnetic responsiveness (Supplementary Fig. 8c).

https://doi.org/10.1038/s41467-024-52347-w

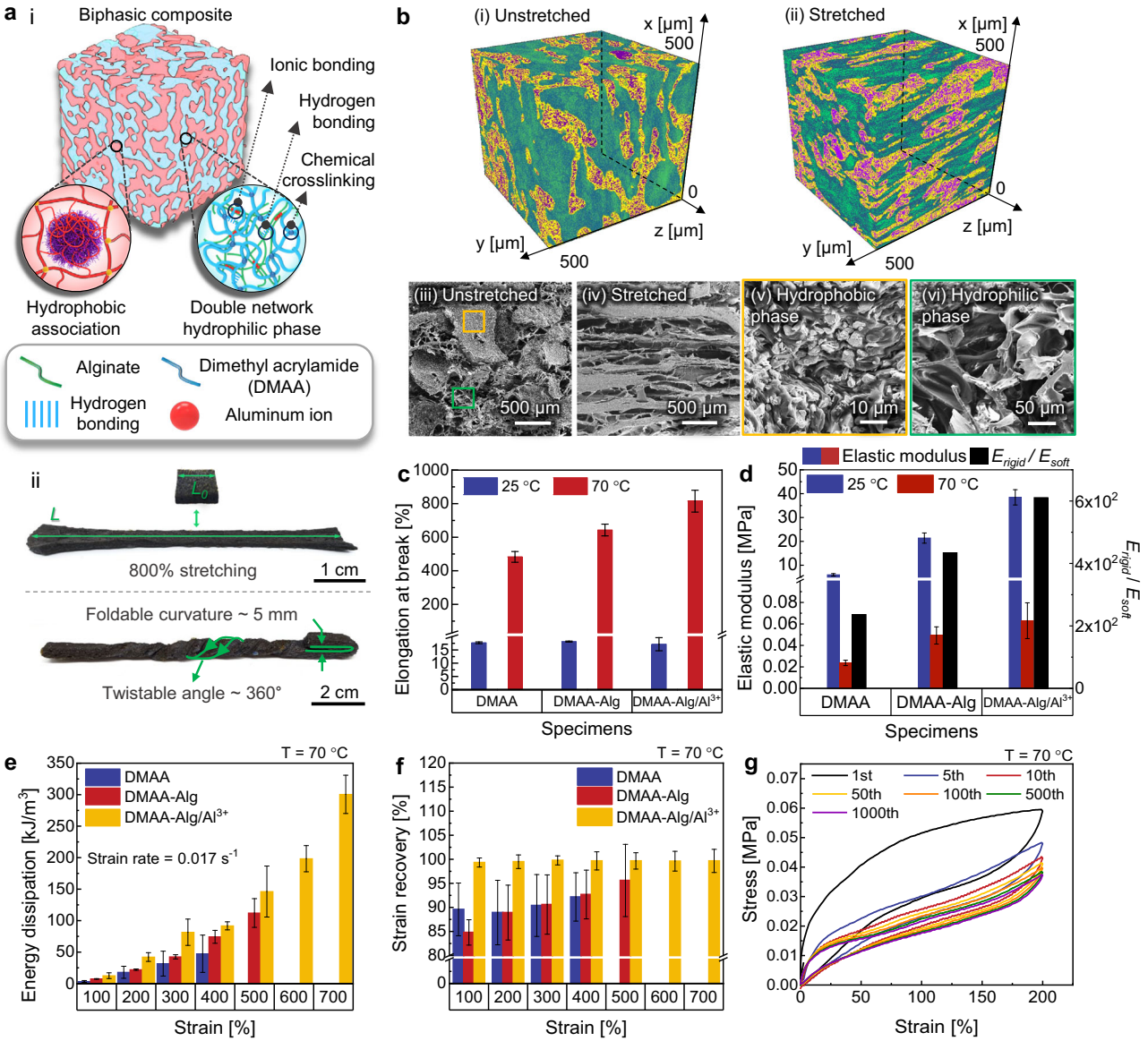

Fig. 3 | Design and properties of the biphasic composite muscle. a (i) A schematic illustration depicting the chemical composition of the biphasic composite and (ii) photographs showing the high deformability of the composite. **b** (i, ii) 3D Nano-CT images of the (i) unstretched and (ii) stretched biphasic composite; (iii, iv) SEM images of the (iii) unstretched and (iv) stretched biphasic composite; and (v, vi) SEM images showing the enlarged view of the (v) hydrophobic and (vi) hydrophilic regions of the biphasic composite. **c** Elongation at break of the three types of biphasic composites at 25 °C and 70 °C. **d** Elastic moduli and stiffness switching ratio of the three types of biphasic composites at 25 °C and 70 °C. **e** Energy dissipation of the three types of composites under strains from 100% to 700% at 70 °C. **f** Strain recovery of the three types of biphasic composite under strain from 100% to 700% at 70 °C. **g** Stress-strain curves of the biphasic composite (DMAA-Alg/Al^{3+}) during 1000 cyclic loading–unloading tests at 70 °C. Error bars in each graph represent standard deviation, $n = 5$ independent samples.

Interestingly, when the monophasic and biphasic composites were sandwiched together— with the right half layer serving as the biphasic composite and the left half layer being the monophasic composite (Supplementary Fig. 18)—the primary strengths of each composite could be integrated while mitigating their respective limitations. As shown in Fig. 4aiii, b and Supplementary Movie 8, the bilayer composite actuator demonstrated rapid actuation with a short settling time of 0.25 s, minimal vibration, and full bending motion with a maximum bending angle of 89°, simultaneously. To quantify the damping performance of the three types of magnetic composites, we evaluated their damping ratio (ζ, the ratio between the actual damping coefficient and the critical damping coefficient) based on a damped sine wave model (Supplementary Note 9). The monophasic composite displayed a ζ of 0.617, indicating underdamped vibration ($\lambda < 1$), while the biphasic composite had a significantly higher ζ of 1.799 ($\lambda > 1$), corresponding to overdamped vibration. In contrast, the bilayer composite had a ζ of 1.348, closer to critical damping ($\lambda = 1$), demonstrating rapid equilibrium without oscillation.

Multifunctional continuum robotic manipulator

As a conceptual demonstration of the proposed monophasic and biphasic composites in soft robotic applications, we fabricated a continuum robotic manipulator comprising two distinct parts: an arm and a multi-fingered hand (Fig. 5a). The arm section utilized a bilayer of the monophasic and biphasic composites to balance field responsiveness, stretchability, and damping capacity. The multi-fingered hand was constructed using a monophasic composite to maximize field responsiveness.

Next, we investigated the quantitative bending and extension behavior of the robotic manipulator in response to an applied

https://doi.org/10.1038/s41467-024-52347-w

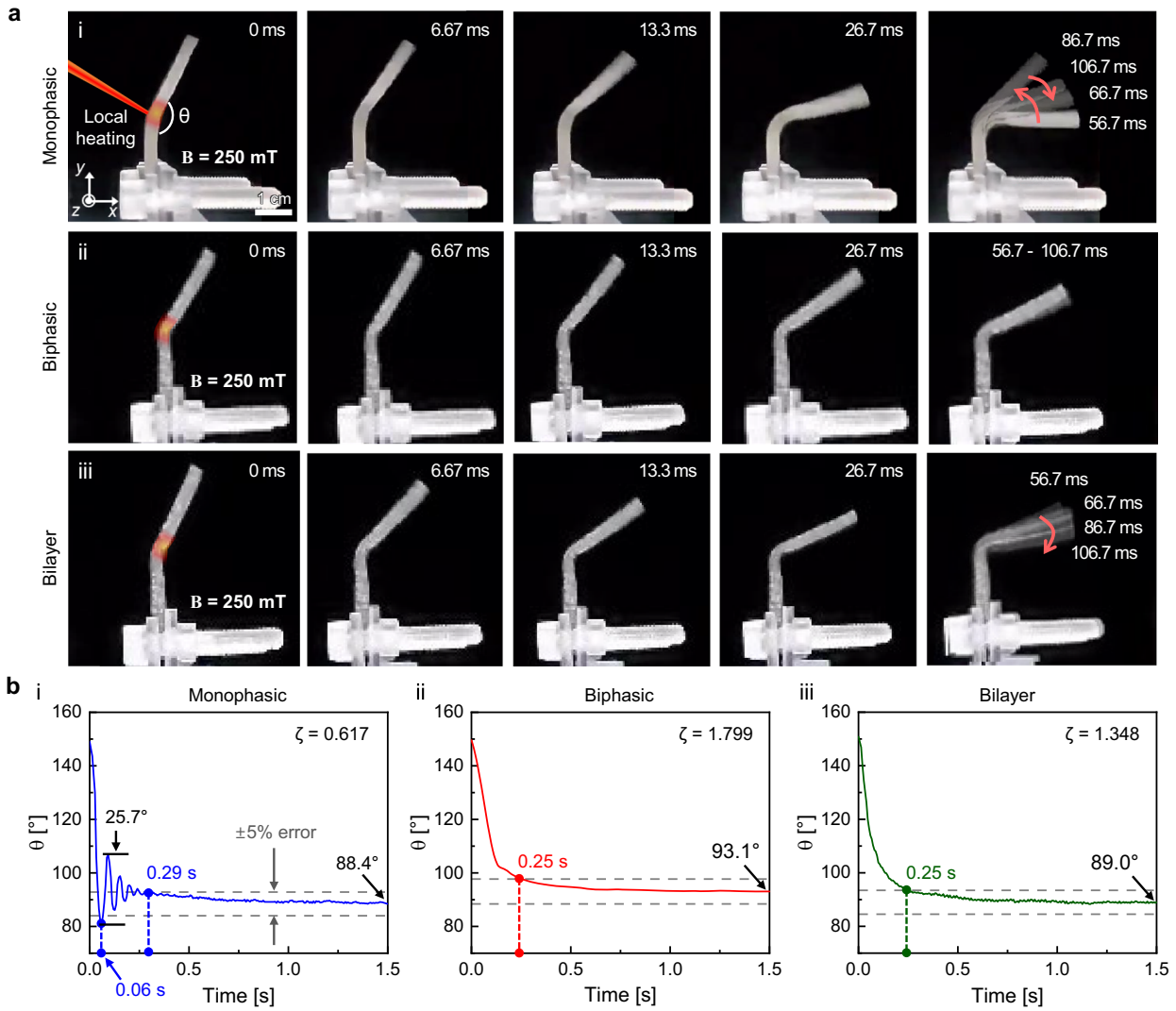

Fig. 4 | Damping capacity of the magnetic composite muscle. a Time-lapse photographs showing the responsive bending actuations of (i) the monophasic composite, (ii) the biphasic composite, and (iii) the bilayer composite muscles. **b** Analyzed bending angles of the (i) the monophasic, (ii) biphasic, and (iii) bilayer composite muscles over time.

magnetic field. To assess the bending angle, we fixed one end of the manipulator to a jig and irradiated the midpoint of the manipulator with a laser at a power density of 2 W cm^{-2}. Subsequently, we applied a magnetic field perpendicular to the length direction of the manipulator, controlling the magnetic flux density. As the flux density increased from 0 mT to 6.3 mT, the bending angle linearly increased to 85.3° (Fig. 5bi). We also explored the extension motion of the robotic manipulator by adjusting the distance between a permanent magnet and the manipulator along its length. This modulation created a change in the magnetic flux density. As the permanent magnet approached the manipulator—from an initial distance of 50 mm down to 0 mm—the flux density increased from 0 mT to 364 mT (Fig. 5bii). Consequently, the manipulator elongated, exhibiting a strain of up to 398%. Additionally, we examined the surface temperature of the robotic manipulator by varying the laser power density from 1.1 to 2.4 W cm^{-2} (Fig. 5c). Laser irradiation at the lowest power density of 1.1 W cm^{-2} raised the surface temperature to 70 °C in just 17 s. With the power density of 2.4 W cm^{-2}, the time required to reach 70 °C was further reduced to 2 s.

Controlled by an electromagnet system integrated with a permanent magnet (see method section and Supplementary Fig. 20 for details), the robotic manipulator was subjected to a sequence of actions (Fig. 5d and Supplementary Movie 9). The manipulator was initially positioned near a target object (red cylinder), with a flat, open hand (Fig. 5di). The objective was to pick up the cylinder and place it into the red hole. To achieve this, the multi-fingered hand was locally heated using an 808 nm laser (irradiance: 2 W cm^{-2}) and then actuated to grasp the cylinder by applying a magnetic field along the x-axis (Fig. 5dii). The infrared image in Figure 5dii, clearly reveals the locally heated and deformable hand. Subsequently, the arm part was stretched by irradiating the entire arm with the laser, followed by field application along the z-axis (Fig. 5diii). The arm elongated successfully while securely holding the object. Next, a specific region of the arm was locally heated with a laser. In this state, applying a magnetic field along the x-axis resulted in bending motion at the heated region, allowing the precise placement of the cylinder on the target delivery point without inducing significant arm vibrations (Fig. 5div). Finally, the actuation of the hand ensured the accurate placement of the cylinder into the target hole (Fig. 5dv).

Notably, the robotic manipulator executed a series of intricate continuous motions, encompassing finger bending, arm extension, local arm bending, and object pick-and-place. The manipulator demonstrated not only bending and extension but also twisting and contracting motions (Supplementary Fig. 21). This diversity of motions

https://doi.org/10.1038/s41467-024-52347-w

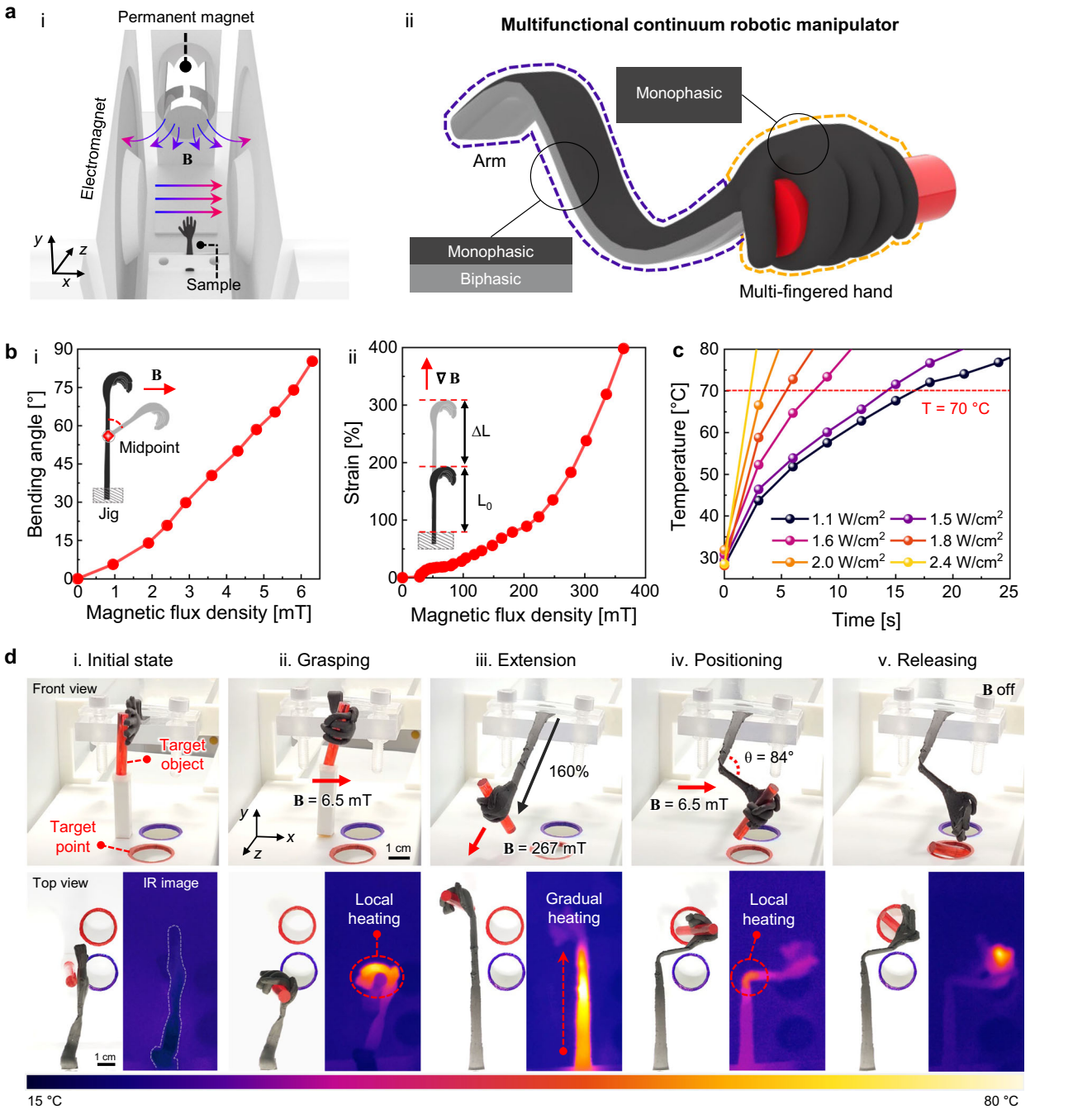

Fig. 5 | Application of the composite muscle to soft continuum robots. a (i) A schematic illustration showing the magnetic field control system used for controlling the robotic manipulator and (ii) a schematic illustration showing the structures of the continuum robotic manipulator. **b** (i) Bending angle and (ii) strain of the robotic manipulator as a function of the applied magnetic flux density. **c** Surface temperature of the manipulator as functions of laser power density and irradiation time. **d** Time-lapse photographs and IR images demonstrating the intricate continuous and sequential actuating motions of grasping, stretching, positioning, and release of the robotic manipulator via the control of selective laser heating and magnetic field control.

transcends the limited actuating modes seen in previous artificial actuators (Supplementary Table 2).

Discussion

In summary, we have introduced artificial muscles that demonstrate complex and reconfigurable actuating modes by integrating phase-changing polymers and ferromagnetic particles in a composite configuration. This design leverages various dynamic reversible bonds in the composite network. As a result, these artificial composite muscles can adjust their mechanical strength from a soft to a rigid state through photothermal stimulation using a laser, achieving an SSR exceeding 2.7×10^3. Consequently, the composite muscle can exhibit versatile dynamic motions under an external magnetic field. It is also capable of sustaining heavy objects with a maximum payload-to-weight ratio of up to 1000 in tensile mode and 3690 in compressive mode. Moreover, the magnetic composite muscle demonstrates improved material and actuation performance. These include a high maximum modulus (2.4 GPa), significant elongation at break (815%), optimal damping ratio (1.348), high actuation strain rate (63.8% s^{-1}), impressive work density (129.5 kJ m^{-3}), and exceptional energy efficiency (90.9%). Importantly, these performances can be tailored by harnessing biphasic polymer networks to enhance energy dissipation,

damping capacity, and stretchability. Due to these remarkable properties, a soft robotic manipulator made of the magnetic composites could successfully perform accurate and complex tasks through remote control.

It is worth noting that the maximum work density of the magnetic composite muscle, at 129.5 kJ m^{-3}, falls within the mid-range of work densities observed in existing soft muscles and actuators (which range from 15.3 to 1700 kJ m^{-3})[35,36]. This occurs because our composite muscle softens to a low modulus (E_{soft}) during actuation and work. Consequently, its liftable weight is limited, resulting in a relatively low work density. However, in this low modulus state, the composite muscle exhibits high stretchability, allowing the lift distance to increase. This compensates for the limited liftable weight, ultimately enabling the composite muscle to achieve a moderate work density (see Supplementary Note 10 and Supplementary Fig. 22 for more details).

While artificial magnetic composite muscles exhibit excellent mechanical and actuation performances, magnetic robots are specialized for operation in confined environments where an external magnetic field is available[55,56]. Consequently, biomedical devices designed to operate within such confined magnetic fields stand to benefit from the unique capabilities of the composite muscle[27,57]. For instance, once their biocompatibility is established, catheters or stents equipped with the ability to actively adjust their mechanical and actuation performance for medical procedures could be developed using the magnetic composite. Furthermore, if efficient remote heating of the magnetic composite can be achieved (e.g., through magnetic radio frequency heating), the utility of the magnetic composite in biomedical applications could be greatly expanded (Supplementary Note 11 and Supplementary Fig. 23). In addition to biomedical applications, the dynamic stiffness controllability offered by the proposed magnetic composite could also be exploited in the development of precise robotic manipulators featuring active adhesion control for applications in precision manufacturing.

Lastly, although we utilized the replica molding technique to prepare the soft robots in this study, direct 3D printing of the magnetic composite will enable more efficient fabrication of soft robots with complex 3D shapes[58]. Additionally, integrating diverse sensors can further enhance the functionalities of magnetic composite robots[59]. With these advancements, along with their exceptional mechanical and actuation properties, the artificial composite muscles presented in this study show immense potential across various fields, including microrobotics, biomedical devices, soft grippers, and bioinspired robotics.

Methods

Materials preparation

NdFeB microparticles (MQFP-B-20076-089) were purchased from Neo Performance Materials (Toronto, Canada). Ammonium hydroxide solution, stearyl methacrylate, ethylene glycol dimethacrylate (EGDMA), azobisiosbutyronitrile (AIBN), *N,N*-dimethylacrylamide (DMAA), alginic acid sodium salt, aluminum chloride, potassium persulfate (KPS), and *N,N,N′,N′*-tetramethylethylenediamine (TEMED) were obtained from Sigma-Aldrich (St. Louis, MO, USA). Tetraethyl orthosilicate (TEOS, 98%) and *N*-Octadecyltriethoxysilane (ODTS, 95%) were purchased from Alfa Aesar (Haverhill, MA, USA). Synthetic phyllosilicate (Laponite RD and RDS) was provided by BYK Additives & Instruments (Wesel, Germany). AIBN was freshly recrystallized from methanol, and other chemicals were used without further purification.

Synthesis of the monophasic composite muscle

To synthesize ODTS-grafted NdFeB microparticles in the monophasic composite, the NdFeB microparticles were subjected to silicate coating using the Stöber method, which involves hydrolysis and condensation. First, 40 g of NdFeB microparticles were dispersed in 1000 mL of ethanol with vigorous stirring at 1000 rpm, using a digital mixer on a hot plate (Daihan Scientific, Korea), to prevent sedimentation. Subsequently, 90 mL of 25% ammonium hydroxide was slowly added to the dispersion, followed by the gradual addition of 3 mL of TEOS and ODTS as droplets after 10 min. The resulting mixture was stirred at room temperature for 12 h. The obtained product was washed three times with ethanol, followed by filtration and drying at room temperature to yield the ODTS-grafted NdFeB microparticles.

To prepare the monophasic composite, a mixture of 52.5 mg EGDMA and 240 mg (1.46 mmol) refined AIBN was added to 52.2 g of stearyl methacrylate under stirring to eliminate any residuals. The synthesized ODTS-grafted NdFeB particles (9 g, 10 g, 11 g, 12 g, and 13 g) were added to 3 mL of the mixture and blended in a heated water bath at 70 °C. The monophasic composite was subsequently synthesized by polymerization at 70 °C for 12 h in a convection oven.

Synthesis of the biphasic composite muscle

The biphasic magnetic composite was synthesized through the in-situ polymerization of Pickering emulsions. Initially, an aqueous phase was formed by adding 0.648 g of laponite RD and 2.73 g of laponite RDS to 27 g of deionized (DI) water. Next, 10 g of DMAA (3.73 M relative to DI water) and sodium alginate (3 mmol) were incorporated into the laponite aqueous solution. Subsequently, 11 g of a monophasic composite was introduced into the aqueous phase at 70 °C. Then, 300 μL of 0.6% KPS and 100 μL of TEMED were added to the mixture. The resulting blend was homogenized at a speed of 800 rpm for 5 min to achieve a stable oil-in-water biphasic matrix. Finally, the biphasic matrix was subjected to radical polymerization at 70 °C for 1.5 h under the protection of N_2. Thereafter, the aluminum ions were uniformly distributed in the crosslinked pristine biphasic gel by soaking it in a 0.05 M solution of aluminum chloride.

Fabrication of the continuum robotic manipulator

A robotic hand was fabricated through thermal curing-assisted molding process with a synthesized monophasic and/or biphasic magnetic composite. An aluminum mold, with a negative hand shape, was prepared by milling using a CNC multi-tasking machine (NTX1000, DMG MORI, Japan). For the single-layered robotic hand, a monophasic magnetic composite was applied to the aluminum mold, with a cover glass to protect it from air contact. Then, the robotic hands were produced through polymerization at 70 °C for 12 h in a convection oven with gentle demolding. For the bilayer robotic hand, the monophasic composite or the biphasic magnetic composite was poured into an aluminum mold one at a time, each occupying half the volume of the mold, followed by thermal curing at 70 °C for 12 h with a cover glass. Subsequently, the robotic hand was demolded from the aluminum mold and immersed in a 0.05 M aluminum solution to substitute Na^+ ions with Al^{3+} ions in the biphasic layer.

Magnetization and analysis of magnetic properties

The magnetic composites were magnetized using a superconducting magnet system (Oxford Instruments, Teslatron PT 14 T, United Kingdom) at the magnetization rates of 100 Oe s^{-1} and magnetic fields of up to 140 kOe. The specimens were prepared by deforming them into specific shapes (e.g., bent, twisted, or curled) to form the desired direction of magnetization inside the magnetic composites and placed in the machine by loading into the cylindrical holder (diameter of 19 mm and height of 25 mm) at 25 °C.

The magnetic hysteresis loops of the magnetic composites were measured using the magnetic property measurement system (Quantum Design, MPMS7, USA) under the controlled temperature conditions of 25 °C and 70 °C with a resolution of 0.3 K. The magnetization and demagnetization rates were set at 100 Oe s^{-1} with a magnetic field change of up to 65 kOe. The root mean square sensitivity was less than 10^{-5} emu. In addition, the permanent magnet and magnetic coil were

characterized using a Gaussmeter (MG-3002, NUTRON, Korea) with a range of 0–2 T and a sensitivity of 0.01 mT.

Actuation control of the continuum robotic manipulator

The soft continuum robot could execute various motion sequences using a custom-built magnetic field control system that combines an electromagnet system and a neodymium permanent magnet (Fig. 5ai and Supplementary Fig. 20). The electromagnet control system consisted of two coils along the X-axis (with an outer diameter of 300 mm and a 100 mm distance between the coils) capable of generating a magnetic field of up to 352 mT (maximum DC output range of 50 V) at the center position and switching the magnetic field direction. The permanent magnets (radius of 50 mm, thickness of 110 mm, and flux density of 0.45 T) were mounted at the end of the Z-axis. Both the electromagnet and the permanent magnet were integrated with a linear bearing, which could slide along the Z-axis.

Applying a magnetic field induces various motions, such as bending, stretching, or twisting. The specific mode and magnitude of the response depend on the distribution and strength of the magnetic field. When a uniform magnetic field is applied to the robot via the electromagnet control system, a magnetic torque ($\vec{\mathbf{T}}_\mathbf{m}$) is generated, which is expressed as follows[60]:

$$\vec{\mathbf{T}}_\mathbf{m} = \vec{\mathbf{m}} \times \vec{\mathbf{B}} \tag{1}$$

Here, $\vec{\mathbf{m}}$ represents the magnetic moment, and $\vec{\mathbf{B}}$ is the magnetic flux density. A strong and agile bending motion can be driven by applying the magnetic torque, which is controlled by adjusting $\vec{\mathbf{B}}$ through a power controllable electromagnet system and by changing the angular alignment between the magnetic field and the robot. On the other hand, applying the gradient of the magnetic field ($\nabla\vec{\mathbf{B}}$) using a permanent magnet generates a magnetic pulling force ($\vec{\mathbf{F}}_\mathbf{m}$), calculated as follows:

$$\vec{\mathbf{F}}_\mathbf{m} = (\vec{\mathbf{m}} \cdot \nabla)\vec{\mathbf{B}} \tag{2}$$

In the magnetic field control system, the stretching motion can be driven by applying $\vec{\mathbf{F}}_\mathbf{m}$, where $\vec{\mathbf{B}}$ is controlled by adjusting the distance between the robot and the permanent magnet mounted on a customized linear bearing. By utilizing both $\vec{\mathbf{T}}_\mathbf{m}$ and $\vec{\mathbf{F}}_\mathbf{m}$ simultaneously or sequentially, multiple locomotion modes can be induced.

Laser heating was utilized to achieve the soft-rigid state phase transitions of continuum robots. The continuous-wave NIR laser (808 nm, 2 Wcm^{-2}, MXL-III-808, UNIOTECH, Korea) was operated at an ambient temperature of 10–35 °C and a initial sample temperature of 25 ± 3 °C. The laser was mounted on the movable jig at the top of the magnetic system, and its position can be fixed or changed to the point of interest, allowing it to irradiate the local target point of the robot to enable selective movement control. Surface temperature was monitored in real-time using an infrared (IR) imaging camera (Xi 400, Optris, Germany).

For motion control, the magnetic field and laser heating were controlled in either manual or automatic mode. In manual control, the permanent magnet and electromagnet were positioned or activated manually to generate the desired workspace and magnetic field. The laser was also manually activated, deactivated, and positioned by the operator to achieve the required local temperature changes. The motion of the robot was recorded from both top and front views using a smartphone (Galaxy Fold 3, Samsung, Korea), while the temperature distribution was simultaneously recorded using the IR camera. The magnetic field and laser heating could also be controlled in automatic mode. For the automatic control of laser heating, initial input conditions such as target temperature, laser power density, and laser irradiating spots were first entered into a LabVIEW program (Supplementary Fig. 24 and Supplementary Fig. 25). Then, the laser started to irradiate the robot, and the robot's temperature was monitored in real-time with the IR camera (Supplementary Movie 10). The laser irradiating spot positions were also automatically controlled via a motorized stage. Once the robot's temperature reached the target temperature, the laser heating was automatically turned off. The field control of the permanent and electromagnets was also controlled via the LabVIEW program. The directions and power of the electromagnet, as well as the xyz positions of the permanent magnets, were automatically controlled via LabVIEW in combination with the laser heating control (Supplementary Fig. 26 and Supplementary Fig. 27).

Reporting summary

Further information on research design is available in the Nature Portfolio Reporting Summary linked to this article.

Data availability

All data supporting the findings of this study are included in the main text and the Supplementary Information. Additional datasets are available from the corresponding author (H.E.J.) upon request.

References

1. Wehner, M. et al. An integrated design and fabrication strategy for entirely soft, autonomous robots. *Nature* **536**, 451–455 (2016).
2. Lee, H. et al. 3D-printed programmable tensegrity for soft robotics. *Sci. Robot.* **5**, aay9024 (2020).
3. Awad, L. N. et al. A soft robotic exosuit improves walking in patients after stroke. *Sci. Transl. Med.* **9**, eaai9084 (2017).
4. Smith, M., Cacucciolo, V. & Shea, H. Fiber pumps for wearable fluidic systems. *Science* **379**, ade8654 (2023).
5. Lu, N. S. & Kim, D. H. Flexible and stretchable electronics paving the way for soft robotics. *Soft Robot* **1**, 53–62 (2014).
6. Song, S. K., Fallegger, F., Trouillet, A., Kim, K. & Lacour, S. P. Deployment of an electrocorticography system with a soft robotic actuator. *Sci. Robot.* **8**, eadd1002 (2023).
7. Narang, Y. S., Vlassak, J. J. & Howe, R. D. Mechanically versatile soft machines through laminar jamming. *Adv. Funct. Mater.* **28**, 1707136 (2018).
8. Shepherd, R. F. et al. Multigait soft robot. *Proc. Natl. Acad. Sci. U.S.A.* **108**, 20400–20403 (2011).
9. Cho, K., Kang, D., Lee, H. & Koh, W. G. Multi-stimuli responsive and reversible soft actuator engineered by layered fibrous matrix and hydrogel micropatterns. *J. Chem. Eng.* **427**, 130879 (2022).
10. Roh, Y. et al. Nature's blueprint in bioinspired materials for robotics. *Adv. Funct. Mater.*, 2306079 (2023).
11. Li, Y. Q., Chen, Y. H., Ren, T. & Hu, Y. Passive and active particle damping in soft robotic actuators. *2018 Ieee International Conference on Robotics and Automation (ICRA)*, 1547-1552 (2018).
12. Yang, B. et al. Reprogrammable soft actuation and shape-shifting via tensile jamming. *Sci. Adv.* **7**, eabh2073 (2021).
13. Zhang, Z. et al. Soft and lightweight fabric enables powerful and high- range pneumatic actuation. *Sci. Adv.* **9**, eadg1203 (2023).
14. Hwang, D., Barron, E. J., Haque, A. B. M. T. & Bartlett, M. D. Shape morphing mechanical metamaterials through reversible plasticity. *Sci. Robot.* **7**, eabg2171 (2022).
15. Wang, W., Yu, C. Y., Serrano, P. A. A. & Ahn, S. H. Shape memory alloy-based soft finger with changeable bending length using targeted variable stiffness. *Soft Robot* **7**, 283–291 (2020).
16. Xie, Z. X. et al. Octopus-inspired sensorized soft arm for environmental interaction. *Sci. Robot.* **8**, eadh7852 (2023).
17. Ze, Q. J. et al. Soft robotic origami crawler. *Sci. Adv.* **8**, eabm7834 (2022).
18. Won, S. et al. Multimodal collective swimming of magnetically articulated modular nanocomposite robots. *Nat. Commun.* **13**, 6750 (2022).

19. Kang, M. et al. Self-assembled artificial nanocilia actuators. *Adv. Mater.* **34**, 2200185 (2022).
20. Alapan, Y., Karacakol, A. C., Guzelhan, S. N., Isik, I. & Sitti, M. Reprogrammable shape morphing of magnetic soft machines. *Sci. Adv.* **6**, eabc6414 (2020).
21. Lu, H. J. et al. A bioinspired multilegged soft millirobot that functions in both dry and wet conditions. *Nat. Commun.* **9**, 3944 (2018).
22. Gu, H. R. et al. Self-folding soft-robotic chains with reconfigurable shapes and functionalities. *Nat. Commun.* **14**, 1263 (2023).
23. Wu, Y. H. et al. Locally controllable magnetic soft actuators with reprogrammable contraction-derived motions. *Sci. Adv.* **8**, eabo6021 (2022).
24. Gao, M., Meng, Y., Shen, C. & Pei, Q. B. Stiffness variable polymers comprising phase-changing side-chains: material syntheses and application explorations. *Adv. Mater.* **34**, 2109798 (2022).
25. Xu, P. F. et al. Conductive and elastic bottlebrush elastomers for ultrasoft electronics. *Nat. Commun.* **14**, 623 (2023).
26. Lobato, N. C. C. et al. Microstructure and chemical stability analysis of magnetic core coated with SILICA and functionalized with silane OTS. *Appl. Surf. Sci.* **505**, 144565 (2020).
27. Kim, Y. & Zhao, X. H. Magnetic soft materials and robots. *Chem. Rev.* **122**, 5317–5364 (2022).
28. Liu, M. Z. et al. Shape morphing directed by spatially encoded, dually responsive liquid crystalline elastomer micro-actuators. *Adv. Mater.* **35**, 2208613 (2023).
29. Mun, J., So, S. & Rho, J. Spectrally sharp plasmon resonances in the near infrared: subwavelength core-shell nanoparticles. *Phys. Rev. Appl.* **12**, 044072 (2019).
30. Xiang, M. Y. et al. Microstructure of bottlebrush poly(n-alkyl methacrylate)s beyond side chain packing. *Polymer* **210**, 123034 (2020).
31. Gao, Y. et al. The effect of hydrophobic alkyl chain length on the mechanical properties of latex particle hydrogels. *RSC Adv* **7**, 44673–44679 (2017).
32. Madden, J. D. W. et al. Artificial muscle technology: physical principles and naval prospects. *IEEE J. Ocean. Eng.* **29**, 706–728 (2004).
33. Haines, C. S. et al. Artificial muscles from fishing line and sewing thread. *Science* **343**, 868–872 (2014).
34. Mu, J. K. et al. Sheath-run artificial muscles. *Science* **365**, 150–155 (2019).
35. Kanik, M. et al. Strain-programmable fiber-based artificial muscle. *Science* **365**, 145–150 (2019).
36. Ma, Y. F. et al. Bioinspired high-power-density strong contractile hydrogel by programmable elastic recoil. *Sci. Adv.* **6**, eabd2520 (2020).
37. Dicker, M. P. M. et al. Light-triggered soft artificial muscles: molecular-Level amplification of actuation control signals. *Sci. Rep.* **7**, 9197 (2017).
38. Foroughi, J. et al. Knitted carbon-nanotube-sheath/spandex-core elastomeric yarns for artificial muscles and strain sensing. *ACS Nano* **10**, 9129–9135 (2016).
39. Kim, I. H. et al. Human-muscle-inspired single fibre actuator with reversible percolation. *Nat. Nanotechnol.* **17**, 1198–1205 (2022).
40. Li, M., Pal, A., Aghakhani, A., Pena-Francesch, A. & Sitti, M. Soft actuators for real-world applications. *Nat. Rev. Mater.* **7**, 235–249 (2022).
41. Martinez, R. V., Glavan, A. C., Keplinger, C., Oyetibo, A. I. & Whitesides, G. M. Soft actuators and robots that are resistant to mechanical damage. *Adv. Funct. Mater.* **24**, 3003–3010 (2014).
42. Zhang, L., Zhao, T. & Liu, M. Bioinspired multiphase gels using spatial confinement strategy. *Acc. Mater. Res.* **5**, 48–63 (2024).
43. Mo, F. N. et al. A highly stable and durable capacitive strain sensor based on dynamically super-tough hydro/organo-gels. *Adv. Funct. Mater.* **31**, 2010830 (2021).
44. Sun, J. Y. et al. Highly stretchable and tough hydrogels. *Nature* **489**, 133–136 (2012).
45. Cazzell, S. A., Duncan, B., Kingsborough, R. & Holten-Andersen, N. Demonstration of environmentally stable, broadband energy dissipation via multiple metal cross-linked glycerol gels. *Adv. Funct. Mater.* **31**, 2009118 (2021).
46. Kang, J. H. et al. Tough and water-insensitive self-healing elastomer for robust electronic skin. *Adv. Mater.* **30**, 1706846 (2018).
47. Li, M. X. et al. Superstretchable, yet stiff, fatigue-resistant ligament-like elastomers. *Nat. Commun.* **13**, 2279 (2022).
48. Shi, L. et al. Highly stretchable and transparent ionic conducting elastomers. *Nat. Commun.* **9**, 2630 (2018).
49. Ze, Q. J. et al. Magnetic shape memory polymers with integrated multifunctional shape manipulation. *Adv. Mater.* **32**, e1906657 (2020).
50. Liu, Y. H. et al. Stiffness variable polymer for soft actuators with sharp stiffness switch and fast response. *ACS Appl. Mater. Interfaces* **15**, 26016–26027 (2023).
51. Su, E., Bilici, C., Bayazit, G., Ide, S. & Okay, O. Solvent-free UV polymerization of-octadecyl acrylate in butyl rubber: a simple way to produce tough and smart polymeric materials at ambient temperature. *ACS Appl. Mater. Interfaces* **13**, 21786–21799 (2021).
52. Park, H. et al. Toughening self-healing elastomer crosslinked by metal-ligand coordination through mixed counter anion dynamics. *Nat. Commun.* **14**, 5026 (2023).
53. Seong, M. et al. 3D printable self-adhesive and self-healing ionotronic hydrogels for wearable healthcare devices. *ACS Appl. Mater. Interfaces* **15**, 11042–11052 (2023).
54. Wang, X., Khara, A. & Chen, C. A soft pneumatic bistable reinforced actuator bioinspired by Venus Flytrap with enhanced grasping capability. *Bioinspiration & Biomimetics* **15**, 056017 (2020).
55. Zheng, Z. Q. et al. Ionic shape-morphing microrobotic end-effectors for environmentally adaptive targeting, releasing, and sampling. *Nat. Commun.* **12**, 411 (2021).
56. Kang, M. S., Lee, D. H. Y., Bae, H. & Jeong, H. E. Magnetoresponsive artificial cilia self-assembled with magnetic micro/nanoparticles. *ACS Appl. Mater. Interfaces* **14**, 55989–55996 (2022).
57. Jung, Y., Kwon, K., Lee, J. & Ko, S. H. Untethered soft actuators for soft standalone robotics. *Nat Commun* **15**, 3510 (2024).
58. Park, S. et al. Bioinspired magnetic cilia: from materials to applications. *Microsystems & Nanoengineering* **9**, 153 (2023).
59. Park, W. et al. A sensorized soft robotic hand with adhesive fingertips for multimode grasping and manipulation. *Soft Robot* **11**, 698–708 (2024).
60. Diller, E., Giltinan, J., Lum, G. Z., Ye, Z. & Sitti, M. Six-degree-of-freedom magnetic actuation for wireless microrobotics. *International Journal of Robotics Research (IJRR)* **35**, 114–128 (2016).

Acknowledgements

This work was supported by the National Research Foundation (NRF) of Korea grant (2021R1A2C3006297, to H.E.J./2022R1A2C3007963, to H.W.P./RS-2024-00407687, to S.M.T.).

Author contributions

MS, KS, SK, and HEJ conceived and designed the experiments. MS, KS, SK, HK, SWL, DKK, JK, and HEJ performed the experiments. MS, KS, SK, HK, SWL, SCV, SK, and HEJ analyzed the data. MS, KS, SK, HK, SWL, SMT, and HEJ contributed materials/analysis tools. MS, KS, SK, HWP and HEJ wrote the drafted manuscript, and all other authors reviewed and edited it.

Competing interests

The authors declare no competing interests.

Additional information

Supplementary information The online version contains supplementary material available at https://doi.org/10.1038/s41467-024-52347-w.

Correspondence and requests for materials should be addressed to Hoon Eui Jeong.

Peer review information *Nature Communications* thanks the anonymous reviewers for their contribution to the peer review of this work. A peer review file is available.